Non-invasive characterization of the manufacturing process of a Nuragic bronze statuette: a Neutron Imaging study

Francesco Cantini [a,b,c,*], Oriol Sans Planell [d], Anders Kaestner [e], Manuel Morgano [f], Filomena Salvemini [g], Marta Porcaro [h,i], Antonio Brunetti [h], Anna Depalmas [h], Lorenzo Giuntini [a,c], Francesco Grazzi [b,c]

[a] *Università degli Studi di Firenze (UNIFI), Sesto Fiorentino, Italy*
[b] *Consiglio Nazionale delle Ricerche, Istituto di Fisica Applicata Nello Carrara (CNR-IFAC), Sesto Fiorentino, Italy*
[c] *Istituto Nazionale di Fisica Nucleare, Laboratorio di Tecniche Nucleari per i Beni Culturali (INFN -Labec), Sesto Fiorentino, Italy*
[d] *Helmholtz-Zentrum Berlin für Materialien und Energie (HZB), Hahn-Meitner-Platz 1, 14109, Wannsee, Germany*
[e] *Paul Scherrer Institut (PSI), Villigen, Switzerland*
[f] *European Spallation Source (ESS), Lund, Sweden*
[g] *Australian Nuclear Science and Technology Organisation, (ANSTO), New Illawarra Rd, Lucas Heights, NSW 2234, Australia*
[h] *Università di Sassari (UNISS), Sassari, Italy*
[i] *Università Roma "La Sapienza" (UNIRoma1), Roma, Italy*

ARTICLE INFO

ABSTRACT

The *Nuragic* civilization (Sardinia, Italy, XVIII–VIII Cen. B.C) developed a flourishing bronze metallurgy. The production of *Nuragic* bronze figurines from Sardinia represents a rich historical archive that provides key information about the iconography, the metal production and casting techniques, and on the development of metallurgy in the Mediterranean basin. Since the question about their manufacturing method remains without definitive answer, the understanding of the Sardinian bronze metallurgy is essential to determine which manufacturing techniques were employed to produce complex bronze artefacts. In the frame of a wider research project relating to *Nuragic* bronzes, four artefacts, three anthropomorphic statuettes (a warrior, a priestess, and an offering figure), and one miniature of a basket, were made available by Museo Nazionale Preistorico "L. Pigorini" (Roma, IT). In this work we present the results of the analyses conducted on a bronze figurine depicting an iconic type of *Nuragic* figure: the Priestess. The analysis was performed using White Beam Neutron Tomography (NT) and Bragg Edge Neutron Transmission (BENT) at the Paul Scherrer Institut (PSI) (Villigen, CH). Neutron techniques are nowadays the only available approach for revealing, non-destructively and with good spatial resolution, the morphological and microstructural properties within the whole volume of solid cast metallic artefacts such as this bronze statuette. This work presents the result of a non-invasive analytical investigation on an archaeological bronze artefact, providing outstanding results: from a quantitative analysis of the composition to an in-depth morphological and microstructural analysis capable of unveiling details on the ancient casting methods of the statuette.

1. Introduction

The Nuragic bronzetti, miniature bronze statuettes typical of the Sardinian Nuragic civilization, were created in the early Iron Age, at the height of the technological development of this civilization and stand as a remarkable testament to the ability of Sardinian metallurgists. These figurines had the function of votive offerings and depicted a wide range of subjects: warriors, wrestlers, priests, craftsmen, mythological figures, various female figures, various types of animals, numerous objects linked to daily life, models of "nuraghe", ships etc. All of them appear outstanding concerning the accuracy of their manufacture, the originality of the subjects and the descriptive details.

It is a precious iconographic source, capable of giving us a very effective and evocative insight into the *Nuragic* world and its knowledge of the techniques of production, processing and casting of metals and the development of metallurgy in the Mediterranean basin (Depalmas,

---

2008; Moravetti et al., 2014; Schiavo and Atzeni, 2005). The present work is dedicated to the study of a statuette which represents a particular iconographic type: a female offering figurine (*priestess*) wearing a cloak, standing with the right hand raised and the left one holding a small bowl (Fig. 1, A). The bronze artefact (inv. 26065) was made available together with three other small bronzes from the *Nuragic* art collection of the "Luigi Pigorini" Ethnographic and Prehistory Museum in Roma (now Museo delle Civiltà). Although this type of artefact has been studied over the time, their production methods are still not clearly defined today. It is therefore of primary interest to try to characterize these objects to obtain clues on the ancient production method. The application of neutron techniques to the non-invasive characterization of archaeological metal artefacts represents, today, one of the most cutting-edge and effective methods for obtaining morphological and microstructural information, useful for the determination of the conservation state, but also capable of revealing details on the manufacturing method (Depalmas et al., 2021; Brunetti et al., 2019; Grazzi et al., 2018; Cantini et al., 2023; Cantini et al., 2023; Salvemini et al., 2020; Grazzi et al., 2021). Two neutron imaging techniques were selected for this study. The analyses were performed using White Beam Neutron Tomography (WB-NT) and monochromatic, energy resolved neutron radiography scan exploiting Bragg Edge Neutron Transmission analysis (BENT). Both experiments were performed at the "Swiss Spallation Neutron Source" (SINQ) at the Paul Scherrer Institut (PSI, Villigen, CH): WB-NT measurement were performed on ICON (Imaging with COld Neutrons) (Kaestner et al., 2011) while monochromatic scan was acquired using BOA (Beamline for neutron Optics and other Approaches) (Morgano et al., 2014).

The same statuette (inv. 26065), which is analysed here, together with another bronze statuette depicting the same stylistic type (Bronze *Nuragic* statuette, inv.783, Musei Reali, Torino, IT (Depalmas, 2018) were investigated with an XRF-MC protocol (X-Ray Fluorescence integrated with Monte Carlo simulations) in a previous work by Brunetti et al. (Brunetti et al., 2022). From this previous study it appears that the two statuettes share many similarities both in terms of their conservation state and in the extrapolated overall alloy composition. Another interesting result, however, concerns the quantity of iron detected by XRF-MC on the surface of the head of both figurines (much more abundant in such area than in the rest of the body). According to Brunetti et. al, the hypothesis of selective corrosion due to natural causes (Archaeological burial environment) must be excluded; the fascinating hypothesis therefore formulated is that this iron-rich layer may have been induced through a voluntary treatment or even that it is possible that a decorative layer was applied, such as iron-based pigments i.e., red ochres.

2. Methods

2.1. White beam neutron tomography

WB-NT allows for a complete morphological study of an artefact as well as for a characterization of microstructural features such as porosity, cracks, density inhomogeneities. The measurement was performed on the ICON beamline exploiting 150 mm × 150 mm Field of View (FoV) with a pixel size of 88 μm. The actual measured resolution of the final reconstructed slices is 120 μm. In addition to the 625 projections, 10 open beam (OB) images were acquired in order to normalize the beam intensity fluctuations, any detector defects, etc.; furthermore, 10 dark current (DC) images to subtract the contribution of the digital electronic detector dark current (thermal noise) were acquired. The whole data set was pre-treated exploiting noise filter Remove Outliers by ImageJ software (Rasband, 2011; Rueden et al., 2017). Subsequently the radiographic stack (projections) was normalized with open beam (OB) images (to correct fluctuations in the beam intensity) and dark current (DC) images according to the relationship:
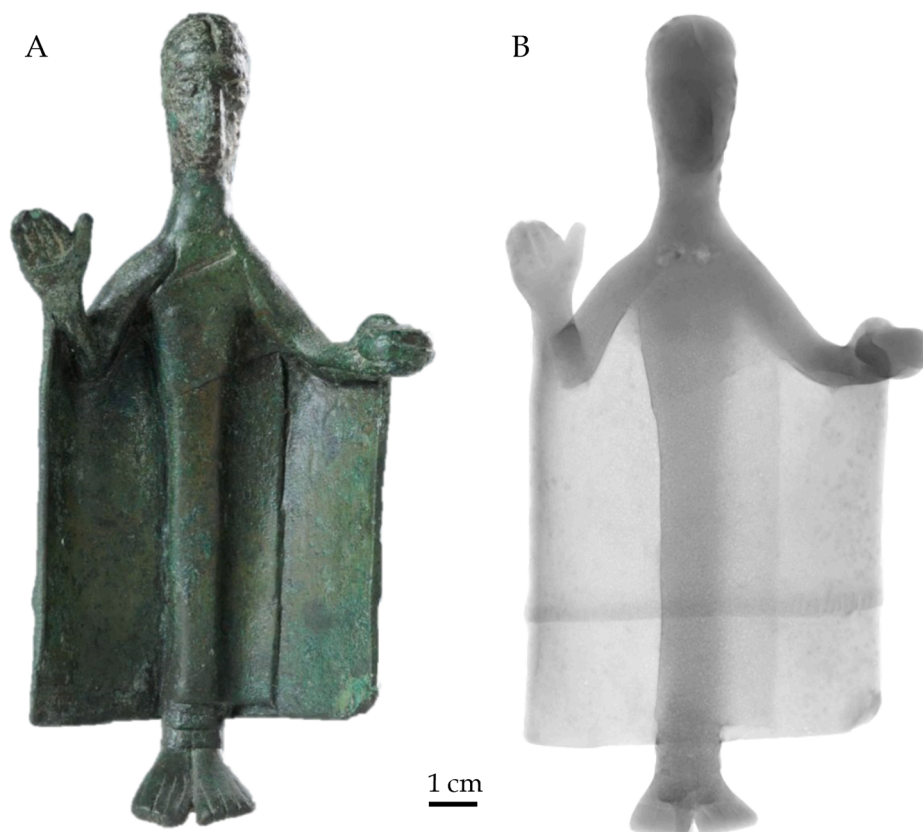

Fig. 1. *Nuragic* bronze statuette from Pigorini Museum n. inv. 26065. (**A**) Photograph; (**B**) Neutron Radiography.

$$I_{norm} = \frac{I_{sample} - I_{DC}}{I_{OB} - I_{DC}} \qquad (1)$$

The Octopus Reconstruction software package (Dierick et al., 2004) was exploited to normalize WB-NT data and for the tomography reconstruction based on Filtered Back Projection algorithm. For visualization, reconstruction of the 3D model, segmentation and quantification of the identified sub-volumes, the open source software 3D-Slicer (Fedorov et al., 2012; Kikinis et al., 2013; 3D-Slicer) was used. Statistical analysis of porosity, such as pore size distribution (PSD) were performed using a method similar to the one used in Salvemini et al., 2023 (Salvemini et al., 2023), employing instead of Thermo-Fisher Avizo 9.3 software, 3D slicer segmentation module (Pinter et al., 2019).

Here is the followed approach:

1) The porosity was segmented, obtaining a 3D model of the pores which we consider the general "porous label" (Fig. 2 a.). With the aim of reconstructing a distribution of pore size in the artefact, it was necessary to divide the volume by separating and grouping the individual pores based either on the number of voxels necessary to describe each unit or on the threshold diameter.

2) The general "porous label" which includes all the pores is refined by eliminating the unresolved particles through a smoothing filter that exploits a median function with Kernel size of 0.176 mm (2x2x2 pixels) (Fig. 2 b.).

3) The following step is the creation of a virtual layered sieve using simple Boolean operations: i) the original "Porous label" is duplicated *n* times depending on how many *n* layers the sieve must have. ii) Since each pore in the segmented volume can be considered an *island* (group of voxels without interconnection with other groups) we can eliminate pores smaller than a certain threshold based on the selected number *m* of voxels. This is equivalent to consider the sieve mesh to be *m* voxels wide. A function that is generally present in segmentation software is "Remove small island", that allows to clean each layer (the new segments) based on an established threshold. For example, if the first layer (segment) contains pores with size > 1000 voxels, and the second with size > 800 voxels, the subtraction of the first segment from the second one returns only the pores defined within a range of 800–1000 voxels. The process can easily be reiterated to obtain different segments each containing a specific group of pores that have the same size.

4) Finally, by attributing a label and a colour to each segment, it is possible to visualise the distribution of the pore size in the artefact. Naturally the fineness of the representation can be refined by decreasing the meshes of the "sieve"(Fig. 2 c., d.).

WB-NT technical details are reported in Table 1.

c. *Virtual sieve layers with different mesh size*

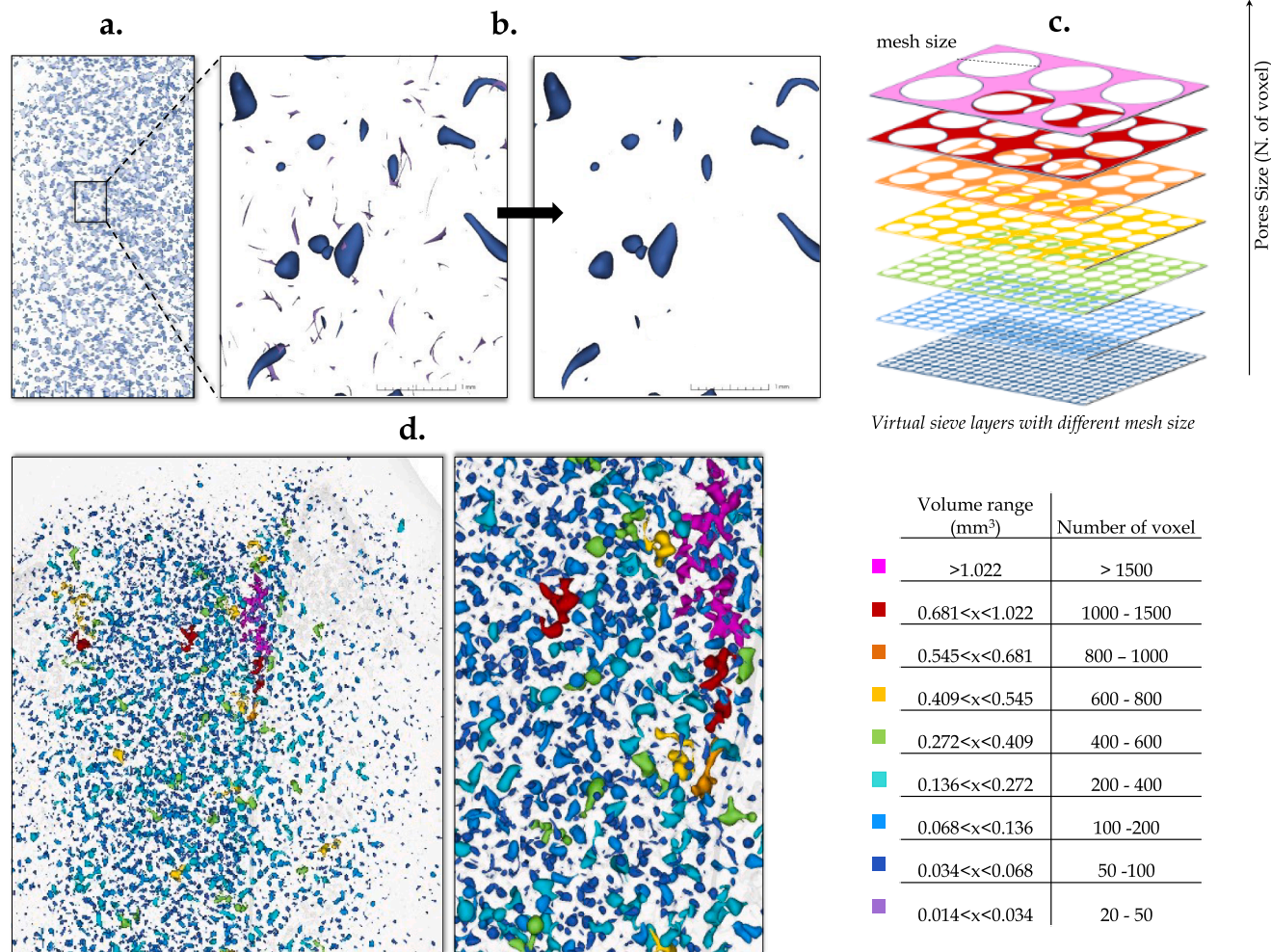| Volume range (mm³)	Number of voxel
>1.022	> 1500
0.681<x<1.022	1000 - 1500
0.545<x<0.681	800 – 1000
0.409<x<0.545	600 - 800
0.272<x<0.409	400 - 600
0.136<x<0.272	200 - 400
0.068<x<0.136	100 -200
0.034<x<0.068	50 -100
0.014<x<0.034	20 - 50

Fig. 2. Workflow of the 3D method for extraction of the pores size distribution inside an artefact. (a) Porosity segmentation; (b) porosity segment refinement; (c) virtual sieve layers organization; (d) visualization and segmentation of pores based on their size.

Table 1
Experimental parameters for the two Imaging facilities used at PSI.

	ICON	BOA
Technique	*White Beam Neutron Tomography*	*Energy Selective Neutron Radiography*
Mean neutron energy	8.53 meV / 3.1 Å	6.67 meV / 3.5 Å
White Beam neutron flux at sample position	1.3×10^7 neutrons $cm^{-2} s^{-1} mA^{-1}$	6.7×10^6 neutrons $cm^{-2} s^{-1} mA^{-1}$
Field of view	150 mm x 150 mm	150 mm x 150 mm
Pixel size	88 μm	63 μm
L/D	343	280
Acquisition time	30–50 s	300 s
Scintillator	GdOx (30 μm)	^{6}LiF – ZnS (Cu) (50 μm)
Monochromator	n.a.	Double Crystal Monochromator (DCM)
Wavelength range	n.a.	2.44 Å – 4.60 Å
Wavelength step Δλ	n.a.	0.02 Å
Number of radiograms	625	109

2.2. Energy selective neutron radiography and Bragg edge neutron transmission analysis

Energy resolved monochromatic neutron imaging can provide a very accurate microstructural characterization. This technique is based on the acquisition of a series of neutron radiographies (or tomographies) at different wavelengths with a monochromatic beam. The use of a monochromatic beam offers the possibility to change the contrast of the image, for the different phases, taking advantage of the abrupt change in the attenuation coefficients at the so-called Bragg cut-off. The attenuation of the intensity of the monochromatic beam induced by the sample depends mainly on two main mechanisms: absorption, and scattering. While the absorption varies linearly with the neutron wavelength, the coherent elastic scattering is related to the polycrystalline structure of the interacting material and can be exploited for contrast enhancement among different phases. In fact, for each crystalline phase, there is a characteristic set of λ ($\lambda = 2d_{hkl}$, where d_{hkl} is the value of a specific lattice plane family pertaining to one of the crystal structures present within the sample) for which the scattering cross section collapses favouring the transmission as described by the well-known Bragg's law. At these λ-values, sharp changes in the intensity transmitted through the sample are observed. The position, extent and broadening of such "edges" thus formed in the transmission profile, can be related to properties as lattice parameters, deformation, grain size and structure, thus providing important information on the crystalline structure of the sample and allowing to obtain clues to the melting temperature or the involvement of cold working in the finishing process of a metal artefact (Santisteban et al., 2002; Sato et al., 2013; Sato, 2017; Grazzi et al., 2010). The position of Bragg edges measured as a function of neutron wavelength is correlated with the lattice plane families of the crystalline specimen according to the following relation:

$$\lambda_{hkl} = 2d_{hkl} \tag{2}$$

where λ_{hkl} is the incident neutron wavelength and d_{hkl} is the distance of the hkl indexed lattice plane family. We acquired 109 monochromatic radiographies (wavelength step Δλ 0.02 Å) in the wavelength range of 2.44 Å − 4.60 Å, which includes the Bragg edges of the families of lattice planes (200) and (1 1 1), of Face centered cubic (FCC) copper. This range is precisely selected to be able to appreciate the highest intensity variations related to the Bragg edges (200) and (1 1 1) for a Cu_α alloy; furthermore, the signal after the Bragg edge (1 1 1) is not correlated to any information on the crystal structure and can be used both as a reference measurement and to visualize microstructural elements such as oligocrystals with strong tonal contrast (Barzagli et al., 2014). A FoV of 150 mm × 150 mm with a 50 μm ^{6}LiF – ZnS (Cu) scintillator was used. Wavelength selection was obtained using Double Crystal Monochromator (DCM) with the crystals arranged horizontally. DCM wavelength gradient results in a shift of the Bragg edge positions along the

horizontal axis of the detector plane (Al-Falahat et al., 2019). To take into account this effect, a Wavelength Radiography scan of a pure copper sample was performed, and the offset of the transmission dip positions was estimated. The offset value was then used to correct our results. Additionally, for comparison measurements of the Sn content, we selected areas aligned along the vertical axis of the figurine. The radiographic stack was filtered and normalized following the same procedure described in the WB-NT. Set up details for Wavelength Selective Neutron radiography are summed-up in the third column of Table 1.

Neutron transmission follows the Lambert-Beer law, therefore the intensity collected in each pixel of the detector panel can be considered representative of the attenuation of the analysed material. The resulting radiography shows an attenuation map in grayscale proportional tones. By acquiring multiple monochromatic radiograms, it is possible to integrate, through the stack, the values of the grey tones as a function of the wavelength, thus obtaining a graph of neutron transmission vs lambda (Fig. 3 A). The transmission profile can be considered complementary to the Bragg edge profile in a plot of total cross section versus lambda. To obtain information about compositional inhomogeneities within the sample, the edges related to the two lattice family planes (200) and (1 1 1) are fit with Boltzmann non-linear function (sigmoidal fit) exploiting Origin (version 2019, Origin Lab Corporation) (Fig. 3 B). By comparing the centroid X_0 of the sigmoidal curve for each transmission edge the presence of a shift can be verified. It is also possible to derive the d-spacing of a specific crystalline plane family: X_0 value (Bragg Edge λ) of the (1 1 1) edge is related to the reticular lattice parameter by the equation:

$$d_{(111)} = \frac{X_0}{2} \times \sqrt{3} \tag{3}$$

X_0 value (Bragg Edge λ) of the (200) edge is also related to the lattice parameter by the equation:

$$d_{(200)} = \frac{X_0}{2} \times 2 \tag{4}$$

This allows to estimate the variation of tin content within the statuette exploiting calibration curve published by Grazzi 2010 (Grazzi et al., 2010), relating equivalent tin concentration with respect to FCC Cu phase lattice parameter increase respect to the pure copper value.

3. Results and discussions

3.1. Morphological analysis

The morphological analysis deriving from the study of WB-NT reconstructions represents a powerful investigative tool as it allows to explore every detail of the investigated volume within the limits of spatial resolution (120 μm). Fig. 4 shows the axial (xy), and normal (zx) tomographic sections of the Statuette (inv. 26065): the artefact, a solid cast bronze, presents no cracks or relevant defects, and apart for the head, seems ubiquitously affected by porosity. In close-up details of the normal (zx) and sagittal (yz) slices (Fig. 5) we observe a strong discontinuity, highlighted by brighter contours, between the head and the body, which indicates that the two parts have been made separately. It is also observed the presence of a diffuse small porosity (average radius: 180 μm) spread all over the whole body from the feet to the neck joint. In correspondence with the neck joint, larger pores (radius range 250 μm – 1.32 mm) can be seen, suggesting the re-cast of the head directly onto the body of the statuette. It is assumed that no complex gating-system (Tarbay, 2020; Hill and Schorsch, 2005) was involved during the head re-casting, and the ventilation channel did not allow for a uniform escape of the gasses that remained trapped in-between the inserting part of the neck and the accommodation volume carved in the chest. The resulting connection of the head resemble a mortise and tenon joint. Looking closely at the junction area, it is evident that the two parts
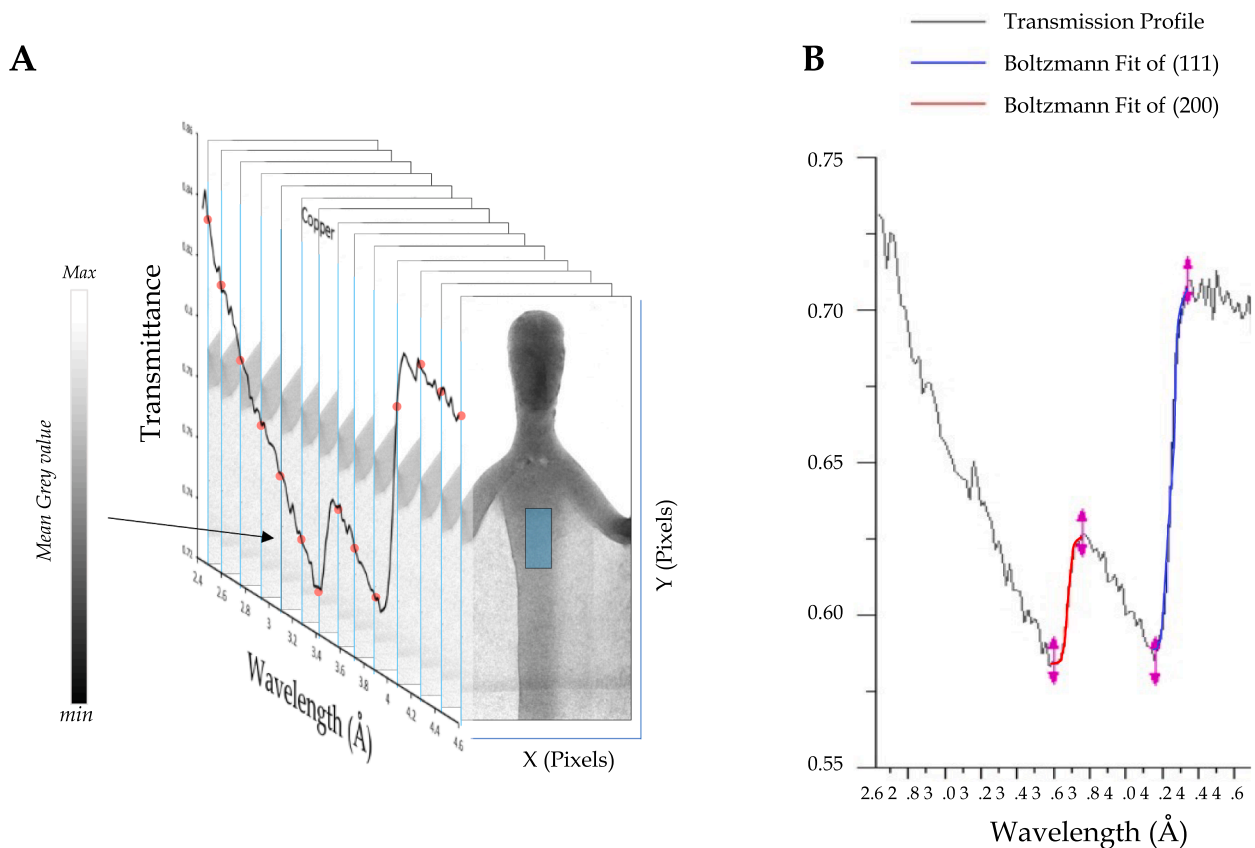
Fig. 3. Diagram of the BENT data analysis procedure. (**A**) A region of the object is selected (blue square). The mean grey value represented inside the square is calculated for all radiograms in the stack. Depending on the wavelength, the mean grey value changes for each radiogram Roi. In the figure, the transmission spectrum as a function of wavelength is superimposed on the side of the radiographic stack. The red dots represent the mean grey value calculated in the blue area for each radiogram. (**B**) Transmittance plot: the blue and red lines represent the Boltzmann fits of the (111) and (200) edges, respectively. Pink double-headed arrows define the ends of each fitting interval range. (For interpretation of the references to colour in this figure legend, the reader is referred to the web version of this article.)
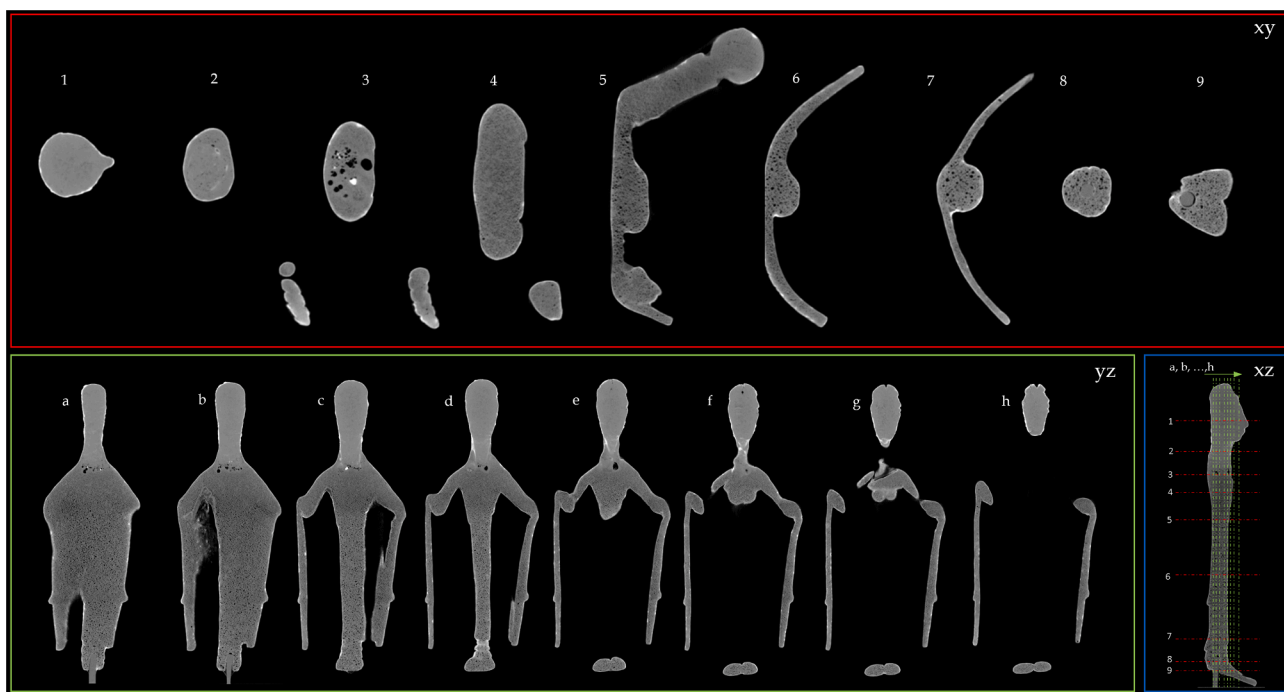
Fig. 4. Neutron tomography: axial (xy) and normal (zx) slices of the "Priestess" (inv. 26065).
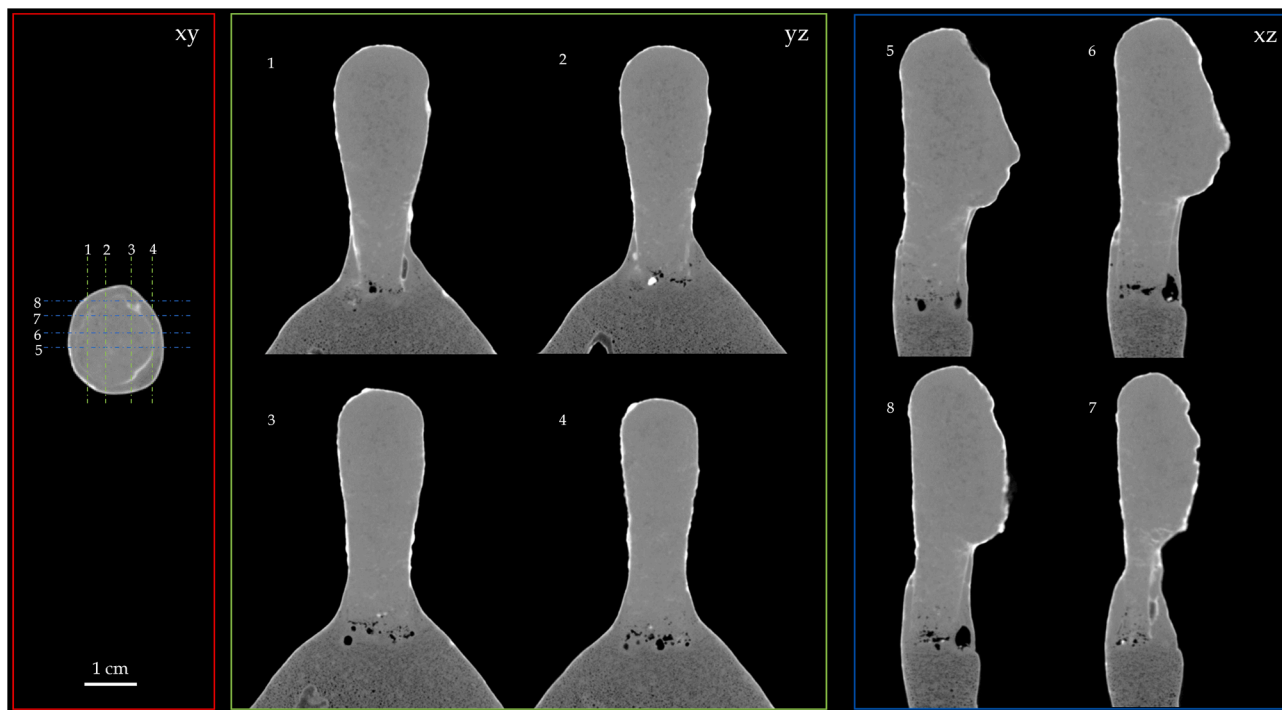
Fig. 5. Neutron tomography: normal (zx) and sagittal (yz) and slices of the "Priestess" (inv. 26065). Detail of the joint between the head and the shoulders.

(the head and the body) merge one into the other in some points. This entails that these areas were undergone to heat treatment, accordingly with the hypothesis that the head wasn't cast separately and then mounted on the body of the statuette, but was cast-on (Bondies et al., 1991; Bavarian and Reiner, 2005) directly on the figurine. The head does not show any porosity, apart from a single bubble of ~ 500 μm radius. The grey tones measured on the head, the neck joint and the main body show some differences, that can be easily explained considering reconstruction artefacts due to the presence of the dense porosity. In fact, during tomography reconstruction, for each pore the alternation of full and empty volumes can induce shadowing effects in the neighbouring area.

The resulting images misleadingly represent these areas as less attenuating. Consequently, the two parts should be made of a similar alloy. Regarding the conservation state, we can establish that the corrosion appears localized on the surface of the artefact and does not

affect the bulk of the statuette. The concretions crusts appear to be thicker on the head (see volume rendering and segmentation in *supplementary material sections S1 and S2*).

Interestingly, as it can be seen in Fig. 4 (xy slice n° 9) under the soles of the feet, a cylindrical cavity houses a small metal bar which served to keep the statuette in position on a pedestal. This element shows no signs of corrosion and even from a visual inspection of the part protruding from the statuette appears to be a steel rod. It is in fact a modern addition which replaced the original pin as confirmed by the curators. Exploiting the volume segmentation, the average volume of corrosion and porosity of the artefact were quantified (Fig. 6). 3D visualization movie and figures of the complete segmentation is available in *supplementary material section S2*.

Moreover, it was possible to calculate the size distribution of the pores inside the statuette (Fig. 7) by exploiting a virtual sieve: this allows to divide and to organize into groups the pores based on their volume
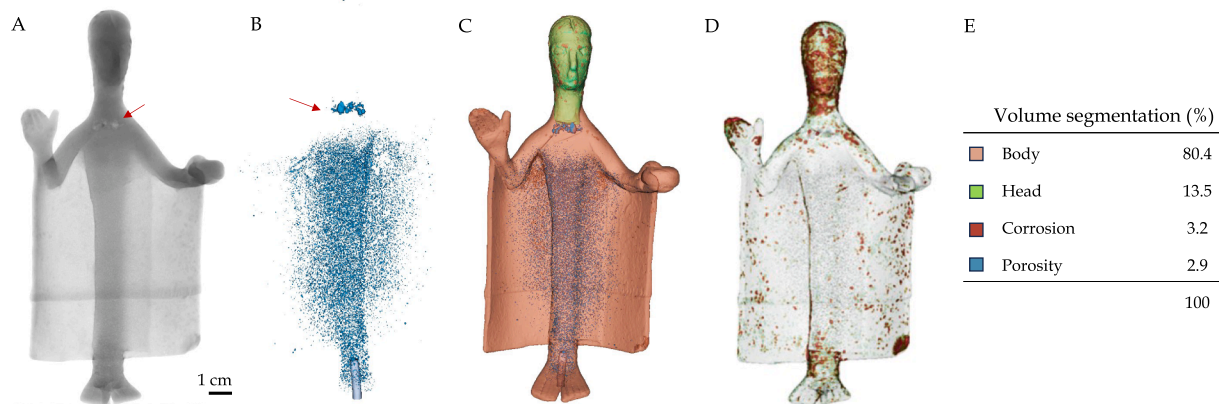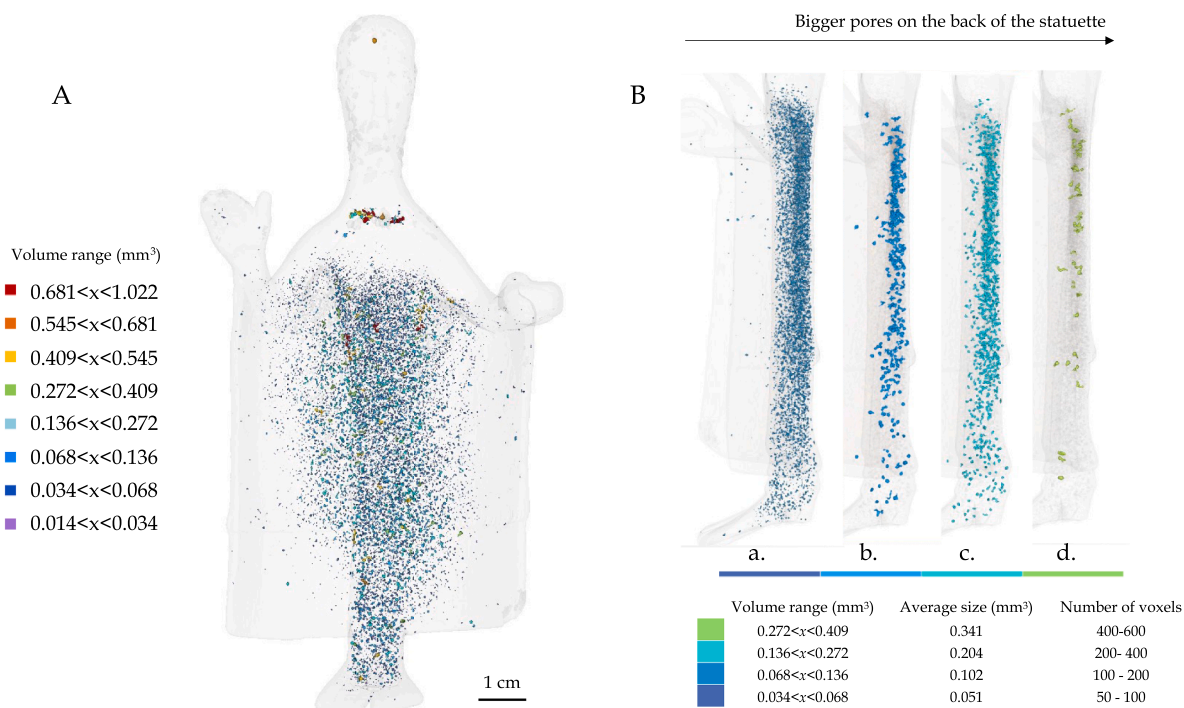

Volume segmentation (%)	
☐ Body	80.4
☐ Head	13.5
☐ Corrosion	3.2
☐ Porosity	2.9
	100

Fig. 6. WB-NT volume segmentation. (**A**) Neutron radiography: the red arrows point to the large cavities under the neck of the statuette; (**B**) segmentation of the porous volume fraction; (**C**) segmentation of the head (green), the body (pink), and the pores (blue); (**D**) Hydrogen rich part (corrosion layer) segmentation. (**E**) Quantification of the different volume segment. (For interpretation of the references to colour in this figure legend, the reader is referred to the web version of this article.)

Fig. 7. Pore size distribution analysis. (**A**) Segmentation of pores of different volume. (**B**) Size distribution of the porous along the profile of the statuette: the selected interval ranges from 50 voxel (0.034 mm³) (**a**) to 600 voxel (0.409 mm³) (**b**).

size. Pores with a volume lower than 0.014 mm³ (equivalent to 20 voxels, 1 voxel = 681472 μm³) were excluded from the segmentation process both because they were close to the spatial resolution limit and because their geometry could not be correctly reproduced with just a few voxels. The extracted pore size distribution is reported in Fig. 7 (A) in false colours, while Fig. 7 (B) shows the selected distribution of pores with a volume ranging from 0.034 mm³ up to 0.409 mm³ along the main body of the figurine. Different colours correspond to different ranges of volume (from a to d). Importantly, it is observed that as the size increases the pores density is higher in the back of the statuette, suggesting that the statuette was cast face down. The reason for the choice of the dimensional range is justified by the fact that pores smaller than 0.034 mm³ are mostly ubiquitous in the main body of the statue, while volumes larger than 0.409 mm³ are only representative of defects such as shrinkage voids or cavities. This type of phenomenon can be observed in the area below the neck (Figs. 5, 6). The complete pores segmentation is available in *supplementary materials section S3*.

Fig. 8 shows the comparison of two close-up radiograms of the head and right hand of the figurine. For each detail two monochromatic neutron radiograms, respectively at λ = 4.12 Å (Fig. 8 A, C) and λ = 4.18 Å (Fig. 8 B, D), around the (111) lattice family plane of Cu FCC, are shown. It is observed that apart from the head, the entire body shows the presence of anisotropic oligocrystals (mm / sub mm scale) which are made up of single-crystalline grains of the Cu-Sn alpha phase oriented in different spatial directions. These appear as dark spots that vanish once the energy edge of the family of lattice planes (1 1 1) has been crossed. This microstructural effect implies that the artefact was slowly cooled, allowing these structures enough time to grow up to the observed size. The distribution and size of these crystals can be particularly significant in providing clues to the process of making the work. The cooling and the solidification of a molten metal during casting starts from the "chilling" walls of the mould and continues towards the core of the metal (Scott, 1991). Smaller thicknesses of metal will cool faster, as seen in the right hand (Fig. 8 C) or mantle areas (cf. *supplementary material S4*). The
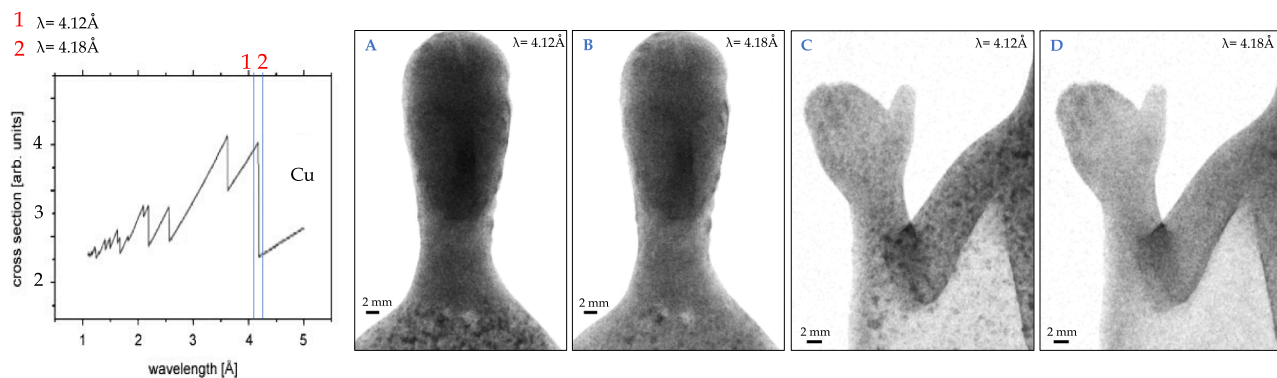
Fig. 8. Monochromatic neutron radiograms around the (111) lattice family plane: (**A**) and (**C**) λ = 4.12 Å; B) and (**D**) λ = 4.18 Å. (**A**) and (**B**) show details of the head of the statuette, (**C**) and (**D**) of the right hand. In the right hand oligocrystals are smaller due to the faster cooling occurred within the thinner parts of the artefact. The plot of the Bragg Edges as function of wavelength of the Cu FCC is shown on the left in the figure, highlighting the two wavelengths at λ = 4.12 Å and λ = 4.18 Å, immediately before and after (respectively) the (1 1 1) Bragg Edge.

head and body are over 1 cm thick and should both have single crystal spots. The absence of this phenomenon in the head imposes different solidification conditions for this part, supporting the hypothesis of a cast-on (fast cooling). Furthermore, observing the neck junction area, it is free of oligocrystals. This could be due to a homogenization phenomenon caused by the contact between the extremity of the cold chest and the molten metal of the re-casting of the head (*for more details refer to supplementary material S4*).

3.2. From a radiographic stack to the quantitative analysis of the alloy

One of the most striking results achieved is the quantitative estimation of the tin equivalent content for the *Nuragic* bronze statuette: the "Priestess". Since XRF-MC analysis in (Depalmas, 2018) highlighted that the head of the figurine show the presence of an iron patina, that is not present in the rest of the body, it was of the maximum importance to compare the elemental composition of the head and of the main body. WB-NI confirms that there is a thick layer of high attenuating material all around the head; moreover, as can be seen in Figs. 4 and 5, the main body and the head share a very similar attenuation coefficient, allowing us to hypothesize that the difference between the alloys should be very small. The transmission profile obtained from BENT data analysis of the head, neck, and body areas is compatible with the Bragg Edge profile of a copper alloy (FCC structure) (Fig. 8, A). If iron would also be present in the bulk of the head, a transmission profile similar to the one of a Body centered cubic (BCC) structure would be expected. The lack of this result confirms what is suggested by those of WB-NT, namely that the high presence of iron-based mineral phases on the head is only superficial. Furthermore, from the BENT analysis we can calculate the d-spacing of peaks pertaining to the FCC Cu-Sn alpha phase relative to the investigated area of the artefact. By integrating the grey value for a specific area of the sample, as a function of the wavelength, the transmission profile is obtained. The transmission profile was fitted with a sigmoidal function whose centroid represents the d-spacing for that peak. Therefore, exploiting the calibration curves published by Grazzi, 2010 (Grazzi et al., 2010), we obtained the equivalent tin content (wt%) for the investigated area (Fig. 9). The differences in terms of concentration of equivalent tin can be explained as the head was cast on the torso and

therefore the two alloys were prepared with the aim of obtaining a similar alloy, but in different time phases of the figurine casting.

3.3. Reconstruction of the casting techniques

The statuette Inv. 26,065 is a solid bronze probably made by direct lost wax casting. WB-NT has proven that the head and the rest of the body belong to two separate castings: it is therefore legitimate to consider that the head is a repair (or an integration) which perhaps even occurred in modern times. This could also partly explain the different chemical nature of the patinas present on the head and on the rest of the body. The fact, however, that there is at least one other example depicting the same iconographic type (the *Nuragic* statuette inv. 783 from Musei Reali of Torino) and that it also presents according to Brunetti et al. (Brunetti et al., 2022) a high concentration of iron only on the head, seems to overshadow this hypothesis. Furthermore, BENT results show that the alloy chosen for the head has a tin content comparable to that present in the rest of the statuette, so it is reasonable to think that the alloy was prepared in a similar way by the same craftsmen. The figurine is a rather small object that could have been made without difficulty in a single casting. It is therefore possible that the artefact, once extracted from the mould, had large defects in the head area, and it was decided to recast it. Looking carefully at the chest area, however, it is possible to notice that the head has not been cast above the shoulders but is inserted into a pre-formed housing to accommodate it. This leads us to suppose that the body may have been deliberately cast without a head.

Looking at the porosity distribution, we can assume that the figurine could be casted upside down but filled from the bottom up. According to this hypothesis, the mould should have had at least a sprue (*S*) positioned at the height of the neck or shoulders to fill the figurine from the bottom up, and a ventilation(*V*) channel positioned above the feet (Fig. 10).

The mould could have been placed slightly tilted into the ground. The three-dimensional reconstruction of the pores (Fig. 10, B) shows that the pores are abruptly interrupted at a precise angle at shoulder height. This may be where the mould was fed with molten bronze, which flowed the gases upwards. Trapped in the molten metal, the gas bubbles
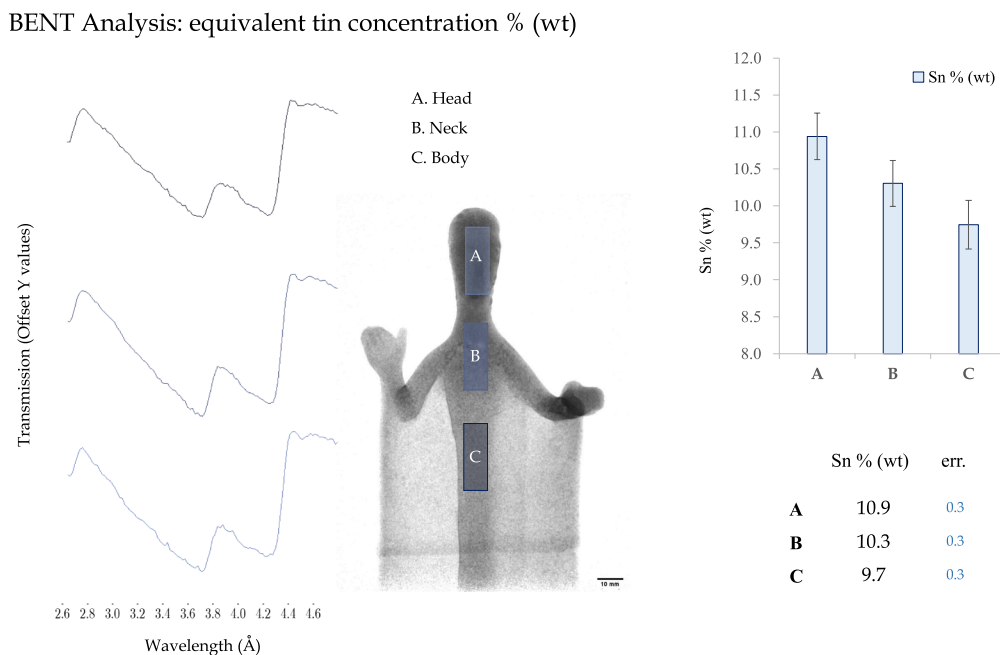
Fig. 9. Results of the BENT analysis conducted on the statuette, showing the equivalent tin content (% wt) of three sample volume A, B and C (10 mm x 10 mm x 20 mm) of the statuette, obtained from the corresponding transmission plots.
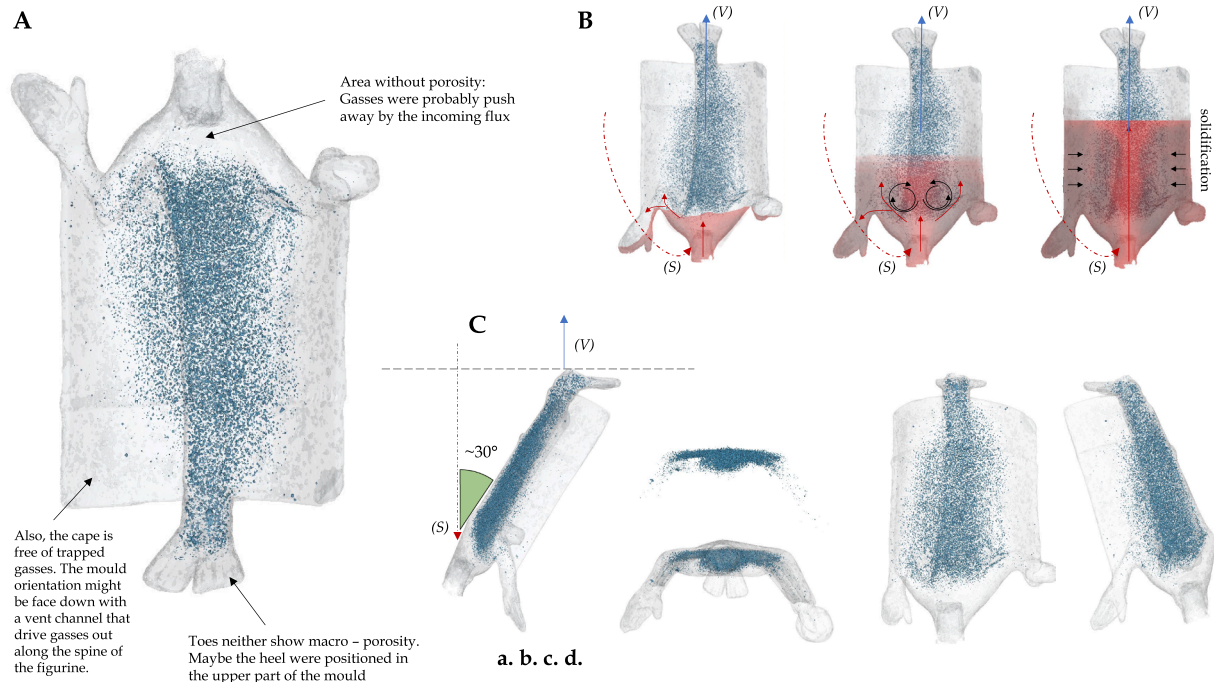
Fig. 10. Casting hypothesis of the statuette. (**A**) In the main body of the statuette, the accumulation of porosity is shown in turquoise: the black arrows point to the areas of the object that appear without pores. Based on the confinement of the pores, it is possible to hypothesize that direct lost wax casting was used exploiting a duct that allowed the mould to be filled from bottom upwards (**B**). Consequently, the figure may have been cast upside down with a main sprue (*S*) at shoulder height and a ventilation channel (*V*) positioned above the feet (**C**). If we then consider the abrupt vertical interruption of the pores at the height of the shoulder blades (**C**, **a.**), and the fact that the farthest point reached by the porosity is in the heels, we can assume that the mould may have been positioned tilted (~30°).

arrange themselves in vertically oriented rows which will be moved upwards following the flow of the incoming bronze (*see supplementary material* S5).

4. Conclusion

In this work, the application of two neutron imaging techniques, WB-NT and BENT, allowed a morphological and microstructural characterization of the *Nuragic* statuette (inv. 26065) in a completely non-invasive way. Exploiting these methods, we were able to evaluate the state of conservation of the artefact by observing that there are no fractures or defects affecting the bulk structure and that the corrosion is mainly limited to the external surface.

The morphological analysis confirmed that the artefact is a solid-cast bronze even if the body of the statue is ubiquitously affected by porosity. It was noted that the head and body were not obtained in a single casting, but the head was probably re-cast in a prepared housing inside the bust. It is assumed that the ventilation system for the mould was not extremely sophisticated and perhaps may have caused a problem with gas accumulation in the area under the neck. This may have led to a shrinkage void that required a second operation to recast the head. Exploiting BENT analysis, we obtained that the casting of the head and body used a slightly different alloy. However, the difference is small enough to suggest that ancient craftsmen prepared the crucible for casting the head with the intent of replicating the alloy used for the main body. This fact, together with the use of the cast-on technique, undoubtedly clarifies the skill and technological refinement that the *Nuragic* civilization craftsmen possessed in the metallurgical field. Furthermore, from the analysis of the monochromatic neutron radiography it was possible to identify spots of oligocrystals of sub millimetric dimensions. This implies that the cooling process of the mould is also a phase that the *Nuragic* foundrymen treated with care.

By segmenting the 3D volume, reconstructed from neutron tomography, it was possible to estimate the volume of the fraction affected by corrosion, the porosity, and the metal. The study of the pore size distribution also allowed us to hypothesize the position of the mould during casting. BENT allowed us to quantify the tin present in the Cu-Sn alpha phase in the body, neck, and head of the statuette. Both the WB-NT and the BENT analysis also confirm that the head is not affected by internal corrosion and therefore all the Fe identified in the previous study by Brunetti et al. (Depalmas, 2018) actually comes from a surface layer. This does not exclude the hypothesis that this corrosion layer may have originally been part of a refined polychrome effect; but obviously this remains a fascinating open question.

CRediT authorship contribution statement

Francesco Cantini: Writing – review & editing, Validation, Supervision, Methodology, Investigation, Formal analysis, Conceptualization. **Oriol Sans Planell:** Writing – review & editing, Investigation. **Anders Kaestner:** Writing – review & editing, Validation, Investigation. **Manuel Morgano:** Writing – review & editing, Investigation. **Filomena Salvemini:** Writing – review & editing, Software. **Marta Porcaro:** Writing – review & editing. **Antonio Brunetti:** Writing – review & editing. **Anna Depalmas:** Writing – review & editing, Resources. **Lorenzo Giuntini:** Writing – review & editing. **Francesco Grazzi:** Writing – review & editing, Validation, Supervision, Methodology, Investigation, Formal analysis, Conceptualization.

Declaration of competing interest

The authors declare that they have no known competing financial interests or personal relationships that could have appeared to influence the work reported in this paper.

Data availability

Data will be made available on request.

Acknowledgments

Appendix A. Supplementary data

Supplementary data to this article can be found online at https://doi.org/10.1016/j.jasrep.2024.104801.

References

3D-Slicer 3D-Slicer, website, 202: https://www.slicer.org/.

Al-Falahat, A.M., Kardjilov, N., Khanh, T.V., Markötter, H., Boin, M., Woracek, R., Manke, I., 2019. Energy-selective neutron imaging by exploiting wavelength gradients of double crystal monochromators—Simulations and experiments. Nucl. Instrum. Methods Phys. Res., Sect. A 943, 162477.

Barzagli, E., Grazzi, F., Salvemini, F., Scherillo, A., Sato, H., Shinohara, T., Zoppi, M., 2014. Wavelength resolved neutron transmission analysis to identify single crystal particles in historical metallurgy. Eur. Phys. J. Plus 129, 1–7.

Bavarian, B., Reiner, L.R., 2005. Piece mold, lost wax & composite casting techniques of the Chinese bronze age.

Bondies, S. D., «Tomography of Ancient Bronzes» in Ancient & historic metals: conservation and scientific research, D. A. Scott, J. Podany e B. B. Considine, editor, Getty Publications, 1991, 75-84.

Brunetti, A., Grazzi, F., Scherillo, A., Minoja, M.E., Salis, G., Orrù, S., Depalmas, A., 2019. Non-destructive microstructural characterization of a bronze boat model from Vetulonia (2019). Archaeol. Anthropol. Sci., 11 (6), pp. 3041–3046.

Brunetti, A., Porcaro, M., Lins, S., di Gennaro, F., Anzalone, R.M., Mineo, M., Depalmas, A., 2022. The strange case of the nuragic offerer bronze statuettes: a multi-analytical study. Materials 15 (12), 4174.

Cantini, F., Scherillo, A., Fedrigo, A., Galeotti, M., Cagnini, A., Porcinai, S., Patera, A., Morandini, F., Grazzi, F., 2023. The Vittoria Alata from Brescia: a combined neutron techniques and SEM-EDS approach to the study of the alloy of a bronze Roman statue. J. Archaeol. Sci. Rep. 51, 104112.

Cantini, F., Creange, S., Li, Y., van Eijck, L., Kardjilov, N., Kabra, S., Grazzi, F., 2023. Morphological and microstructural characterization of an ancient Chola bronze statuette by neutron based non-invasive techniques. Archaeol. Anthropol. Sci. https://doi.org/10.21203/rs.3.rs-3706226/v1.

Depalmas, A., 2018. La scoperta della civiltà nuragica. In: Carlo Alberto Archeologo in Sardegna, 1st ed.;. Nautilus: Beinsaco (To), Italy, pp. 46–65.

Depalmas, A., Cataldo, M., Grazzi, F., Scherillo, A., Fedrigo, A., Kockelmann, W., di Gennaro, F., Canu, A., Brunetti, A., 2021. Neutron-based techniques for archaeometry: Characterization of a Sardinian boat model. Archaeol. Anthropol. Sci. 13 (6), 101.

Depalmas, A., 2008. La figura umana nell'arte nuragica. In Il segno e l'idea. Arte Preistorica in Sardegna, Tanda, G., Lugliè, C. eds, CUEC, Italy, pp. 273-296.

Dierick, M., Masschaele, B., Van Hoorebeke, L., 2004. Octopus, a fast and user-friendly tomographic reconstruction package developed in LabView®. Meas. Sci. Technol. 15 (7), 1366.

Fedorov, A., Beichel, R., Kalpathy-Cramer, J., Finet, J., Fillion-Robin, J.C., Pujol, S., Bauer, C., Jennings, D., Fennessy, F., Sonka, M., Buatti, J., Aylward, S., Miller, J.V., Pieper, S., Kikinis, R., 2012. 3D slicer as an image computing platform for the quantitative imaging network. Magn. Reson. Imaging 30 (9), 1323–1341.

Grazzi, F., Bartoli, L., Siano, S., Zoppi, M., 2010. Characterization of copper alloys of archaeometallurgical interest using neutron diffraction: a systematic calibration study. Anal. Bioanal. Chem. 397, 2501–2511.

Grazzi, F., Brunetti, A., Scherillo, A., Minoja, M.E., Salis, G., Orrù, S., Depalmas, A., 2018. Non-destructive compositional and microstructural characterization of Sardinian Bronze Age swords through neutron diffraction. Mater Charact 144, 387–392.

Grazzi, F., Cantini, F., Morgano, M., Busi, M., Park, J.S., 2021. Microstructural characterization of a single crystal copper rod using monochromatic neutron radiography scan and tomography: a test experiment. Appl. Sci. 11 (16), 7750.

Hill, M., Schorsch, D., 2005. The Gulbenkian torso of King Pedubaste: Investigations into Egyptian large bronze statuary. Metrop. Mus. J. 40, 163–196.

Kaestner, A.P., Hartmann, S., Kühne, G., Frei, G., Grünzweig, C., Josic, L., Schmid, F., E. H. Lehmann a& Lehmann, E. H., 2011. The ICON beamline–A facility for cold neutron imaging at SINQ. Nucl. Instrum. Methods Phys. Res., Sect. A 659 (1), 387–393.

Kikinis, R., Pieper, S.D., Vosburgh, K.G., 2013. 3D Slicer: a platform for subject-specific image analysis, visualization, and clinical support. In Intraoperative imaging and image-guided therapy (pp. 277-289). New York, NY: Springer New York.

La Sardegna Nuragica - storia e materiali, Moravetti A., Alba E., Foddai L. eds, (2014) Carlo Delfino editore, Italy.

Morgano, M., Peetermans, S., Lehmann, E.H., Panzner, T., Filges, U., 2014. Neutron imaging options at the BOA beamline at Paul Scherrer Institut. Nucl. Instrum. Methods Phys. Res., Sect. A 754, 46–56.

Pinter, C., Lasso, A., Fichtinger, G., 2019. Polymorph segmentation representation for medical image computing. Comput. Methods Programs Biomed. 171, 19–26.

Rasband, W.S., 2011. Imagej. http://imagej. nih. gov/ij/.

Rueden, C.T., Schindelin, J., Hiner, M.C., DeZonia, B.E., Walter, A.E., Arena, E.T., Eliceiri, K.W., 2017. Image J2: ImageJ for the next generation of scientific image data. BMC Bioinf. 18, 1–26.

Salvemini, F., Williams, A., Edge, D., Schillinger, B., Cantini, F., Grazzi, F., 2020. On the use of neutron imaging methods to identify microstructural features in ancient Indian swords and armour. Microchem. J. 159, 105397.

Salvemini, F., Pastuovic, Z., Stopic, A., Kim, M.J., Gatenby, S., 2023. An insight into a Shang dynasty bronze vessel by nuclear techniques. Appl. Sci. 13 (3), 1549.

Santisteban, J.R., Edwards, L., Fitzpatrick, M.E., Steuwer, A., Withers, P.J., Daymond, M. R., Johnson, M.W., Rhodes, N., Schooneveld, E.M., 2002. Strain imaging by Bragg edge neutron transmission. Nucl. Instrum. Methods Phys. Res., Sect. A 481 (1–3), 765–768.

Sato, H., 2017. Deriving quantitative crystallographic information from the wavelength-resolved neutron transmission analysis performed in imaging mode. J. Imaging 4 (1), 7.

Sato, H., Shinohara, T., Kiyanagi, R., Aizawa, K., Ooi, M., Harada, M., Oikawa, K., Maekawa, F., Iwase, K., Kamiyama, T., Kiyanagi, Y., 2013. Upgrade of Bragg edge analysis techniques of the RITS code for crystalline structural information imaging. Phys. Procedia 43, 186–195.

Schiavo, F.L., Atzeni, C., 2005. Archaeometallurgy in Sardinia: from the origins to the beginning of the early Iron Age., Schiavo F. L.; Giumlia-Mair A.; Sanna U.; and Valera R. Eds, Les éditions Mergoil, France.

Scott, D.A., 1991. Metallography and Microstructure of Ancient and Historic Metals; The J. Paul Getty Trust: Marina del Rey, CA, USA.

Tarbay, J.G., 2020. Reverse engineering of a bronze age socketed axe. Mater. Sci. Eng. 45 (1), 217–226.